Journal of Physics D: Applied Physics

PAPER

An improved spin readout for nitrogen vacancy center ensemble based on a maximum likelihood estimation method

To cite this article: Jixing Zhang *et al* 2020 *J. Phys. D: Appl. Phys.* **53** 455305

IOP Publishing
Journal of Physics D: Applied Physics
J. Phys. D: Appl. Phys. **53** (2020) 455305 (11pp)
https://doi.org/10.1088/1361-6463/aba7de

An improved spin readout for nitrogen vacancy center ensemble based on a maximum likelihood estimation method

Jixing Zhang[1], **Lixia Xu**[1,7], **Tao Shi**[2], **Guodong Bian**[1], **Pengcheng Fan**[1], **Mingxin Li**[1], **Peirong Chen**[1], **Chang Xu**[1], **Ning Zhang**[3] and **Heng Yuan**[1,4,5,6,7]

[1] School of Instrumentation and Optoelectronic Engineering, Beihang University, Beijing 100191, People's Republic of China
[2] Research Center of Quantum Precision Measurement and Sensors, Hangzhou Innovation Institute of Beihang University, Hangzhou 310051, People's Republic of China
[3] Zhejiang Lab, Hangzhou 310000, People's Republic of China
[4] Research Institute of Frontier Science, Beihang University, Beijing 100191, People's Republic of China
[5] Beijing Advanced Innovation Center for Big Data-Based Precision Medicine, Beihang University, Beijing 100191, People's Republic of China
[6] Beijing Academy of Quantum Information Sciences, Beijing 100193, People's Republic of China

E-mail: hengyuan@buaa.edu.cn and xulixia@buaa.edu.cn

Received 17 May 2020, revised 15 July 2020
Accepted for publication 21 July 2020
Published 19 August 2020

Abstract
In this work, a spin readout method using fluorescence dynamics is proposed based on maximum likelihood estimation (MLE) for improving the pulsed spin readout accuracy of nitrogen vacancy (NV) center. This estimation method can saturate the Cramér–Rao bound and enhance the photon-shot-noise-limited spin readout accuracy by 20% compared with conventional photon summation method. By employing a rate equation model of the NV center, the exact solution for the fluorescence dynamics is obtained. Additionally, according to the rate equation model's relationship with fluorescence dynamics, spin, and pumping light power, a practical MLE readout scheme is furnished, which is able to distinguish spin readout information and classical noise. Compared with the conventional method, the classical noise suppression capability can be improved by 300 times. It is anticipated that the MLE method will effectively benefit sensing capability based on the NV centers even other scalable defect complexes in solid systems.

Keywords: nitrogen vacancy center, photon shot noise, spin readout, maximum likelihood estimation

(Some figures may appear in colour only in the online journal)

1. Introduction

Quantum sensing based on diamond nitrogen-vacancy (NV) centers has broad prospective applications due to its excellent coherence time and physical properties. Some of these applications include magnetic field sensing [1–3], temperature sensing [4, 5], nanometer-scale biomedical measurements [6, 7], and microwave measurements [8, 9]. The electronic spin projection readout of the NV center is the basis of the above quantum sensing techniques, where the readout precision determines the sensing accuracy. The most conventional approach for NV center electron spin readout is utilizing spin-dependent fluorescence [10]. In order to improve the spin readout, a variety of techniques have been proposed. Some of these techniques include improving light collection efficiency [11, 12] and microwave efficiency [13, 14]. As well, spin readout schemes have been proposed based on different principles such as low-temperature resonant excitation

[7] Author to whom any correspondence should be addressed

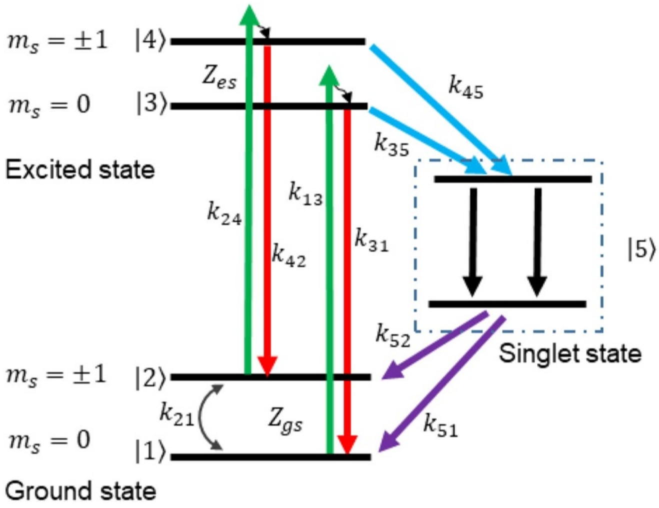

Figure 1. Energy structure of NV center.

readout [15], electric spin readout [16], and infrared singlet absorption [17]. Post-processing methods have also been proposed such as photon summation (PS) [18], threshold detection [10], nuclear-assisted readout [19], maximal adaptive-decision making [20], machine learning [21], and signal extraction using a lock-in amplifier [22, 23]. Some of these methods are only applied to continuous-wave (CW) measurement methods [22–25], while others can only be used for spin–qubit readout [19–21]. Pulsed spin readout is primarily based on PS method. There are two main problems with the PS method. First, the spin readout accuracy of the pulse measurement is limited by the photon shot noise which is fundamentally limited by Cramér–Rao bound [26]. By applying the Cramér–Rao inequality, PS method is not the solution with the smallest variance, nor the optimal solution. Second, for actual experimental systems, classical noise such as laser noise and detector noise further worsen actual spin readout accuracy than the theoretical limit. Therefore, it is important to propose a method that can improve the sensitivity limit and suppress classical sources of noise. In this work, we present a spin readout scheme based on maximum likelihood estimation (MLE). Subsequently, a practical MLE (pMLE) method using multiparameter estimation is developed to suppress further the classical noise existing in actual experimental equipment.

2. Model

A five-level model is furnished to model the optical dynamics of the NV center [27, 28]. As shown in figure 1, at room temperature, the ground state is an $S = 1$ spin-triplet with a zero-field split ($Zgs = 2.87$ GHz) between substate |1> ($m_s = 0$) and substate |2> ($m_s = \pm 1$). The excited state is also a spin-triplet with two substates |3> ($m_s = 0$) and |4> ($m_s = \pm 1$). In the excited state, decay occurs through two paths. These paths are (a) a radiative decay to the ground state with emission of photons at a rate of $k_{31} = k_{42} = k$ and (b) a non-radiative decay to the singlet state |5> with spin-dependent rates of k_{35} and k_{45} [29, 30]. The pumping rate $k_{13} = k_{24} = \Gamma$ from the ground state to the excited state is proportional to the laser power density. Here, $k_p = \Gamma / k$ is introduced for simplicity. The singlet state also spin-dependently decays to the ground state, whose rates are denoted as k_{51} and k_{52}. All relaxation rate parameters are selected based in [31]. Between two substates |1> and |2>, there is longitudinal relaxation time T_1 and we denote $k_{21} = 1/T_1$. The decoherence time T_2 affects the spin coherent states and does not affect the spin projection result, so T_2 is not considered in the spin readout process. The rate equations could be written in terms of ρ_i, which represents population of substate |i>.

$$\begin{aligned}
\frac{d\rho_1}{dt} &= -k_p k \rho_1 + k\rho_3 + k_{51}\rho_5 - \frac{k_{21}}{2}\rho_1 + \frac{k_{21}}{2}\rho_2 \\
\frac{d\rho_2}{dt} &= -k_p k \rho_2 + k\rho_4 + k_{52}\rho_5 - \frac{k_{21}}{2}\rho_2 + \frac{k_{21}}{2}\rho_1 \\
\frac{d\rho_3}{dt} &= k_p k \rho_1 - k\rho_3 - k_{35}\rho_3 \\
\frac{d\rho_4}{dt} &= k_p k \rho_2 - k\rho_4 - k_{45}\rho_4 \\
\frac{d\rho_5}{dt} &= k_{35}\rho_3 + k_{45}\rho_4 - k_{51}\rho_5 - k_{52}\rho_5 .
\end{aligned} \tag{1}$$

Equation (1) is written as, $\vec{\rho}\,' = A \cdot \vec{\rho}$, where $\vec{\rho} = (\rho_1, \rho_2, \rho_3, \rho_4, \rho_5,)^T$ and

$$A = \begin{bmatrix} -k_p k - \frac{k_{21}}{2} & \frac{k_{21}}{2} & k & 0 & k_{51} \\ \frac{k_{21}}{2} & -k_p k - \frac{k_{21}}{2} & 0 & k & k_{52} \\ k_p k & 0 & -k - k_{35} & 0 & 0 \\ 0 & k_p k & 0 & -k - k_{45} & 0 \\ 0 & 0 & k_{35} & k_{45} & -k_{51} - k_{52} \end{bmatrix}. \tag{2}$$

We use E_1, E_2, E_3, E_4, and E_5 to denote the eigenvalues of A. Correspondingly, the eigenvectors of A are denoted as $U_i = (u_i^1, u_i^2, u_i^3, u_i^4, u_i^5)^T$. And set,

$$w_j^i = \left(\begin{bmatrix} U_1 & \cdots & U_5 \end{bmatrix}^{-1} \right)_{ij}. \tag{3}$$

The vector form of the initial state is, $\vec{\rho}(0) = (P, 1-P, 0, 0, 0)^T$. Here, P is the spin projection of the ground state, and estimating method of the parameter P is the essence of this work. The special solution of equation (1) is,

$$\rho_j(t) = P \sum_{i=1}^{5} e^{E_i t} u_i^j w_1^i + (1-P) \sum_{i=1}^{5} e^{E_i t} u_i^j w_2^i . \tag{4}$$

We define $f(P,t)$ as the fluorescence probability density function of a single NV center at a certain time t, that is, the probability of emitting photons at a certain time. It is proportional to the excited state population [31]:

$$\begin{aligned}
f(P,t) = k(\rho_3 + \rho_4) = kP \sum_{i=1}^{5} e^{E_i t} \left(u_i^3 + u_i^4\right) w_1^i \\
+ k(1-P) \sum_{i=1}^{5} e^{E_i t} \left(u_i^3 + u_i^4\right) w_2^i .
\end{aligned} \tag{5}$$

The unit of $f(P,t)$ is counts per second. In order to simplify the subsequent derivation process, we define,

$$\alpha(t) = k\sum_{i=1}^{5} e^{E_i t}\left(u_i^3 + u_i^4\right)\left(w_1^i - w_2^i\right) \tag{6}$$

and,

$$\lambda(t) = k\sum_{i=1}^{5} e^{E_i t}\left(u_i^3 + u_i^4\right)\left(w_2^i\right). \tag{7}$$

In this way, equation (5) can be simplified to:

$$f(P,t) = \alpha(t)P + \lambda(t). \tag{8}$$

μ_n is defined as the total number of photons collected by the detector from time t_{n-1} to time t_n. The subscript integer n represents the nth time tagger, starting from 0, representing the start time of the light pulse. This time interval $t_n - t_{n-1}$ remains unchanged, denoted by Δt. According to this definition, there is a relationship between $f(P,t)$ and expectation of μ_n:

$$CM\int_{t_{n-1}}^{t_n} f(P,t)\,dt = \langle\mu_n\rangle. \tag{9}$$

There, C stands for collection efficiency and M stands for the number of NV centers. A new parameter $\beta = CM$ is defined and it represents the parameters of the optical system and the number of NV center. It can be obtained by the ratio of the excited state steady-state solution $f(t_n \to \infty)\,\Delta t$ to the measured photon number $\mu_{t_n\to\infty}$. According to the definition of f, during the period from t_{n-1} to t_n, the expectation of the number of photons emitted by a single NV center, denoted by F_n, is the integral of the fluorescence probability density during this period:

$$F_n = \int_{t_{n-1}}^{t_n} f(P,t)\,dt. \tag{10}$$

In order to simplify the subsequent derivation process, we define:

$$\overline{\alpha}_n = \frac{\int_{t_{n-1}}^{t_n}\alpha(t)\,dt}{\Delta t} \tag{11}$$

and,

$$\overline{\lambda}_n = \frac{\int_{t_{n-1}}^{t_n}\lambda(t)\,dt.}{\Delta t} \tag{12}$$

Then, equation (9) can be rewritten as,

$$\beta F_n = \beta\Delta t\left(\overline{\alpha}_n P + \overline{\lambda}_n\right) = \langle\mu_n\rangle. \tag{13}$$

From the equation (13), there is a linear relationship between P and $\langle\mu_n\rangle$. Therefore, the conventional PS method, which is to summate the photons of the first hundreds of nanoseconds of the detection pulse $\sum_{n=1}^{n=N}\mu_n$ [3], must also satisfy a linear relationship with P, where N represents total number of measuring points. $T_N = N\Delta t_n$ is the total detection time. In addition, the physical meanings of $\overline{\alpha}_n$ and $\overline{\lambda}_n$ can be reflected from equation (13). Among them, $\overline{\lambda}_n$ represents the spin-independent part in fluorescence, and $\overline{\alpha}_n$ represents the spin-dependent part in fluorescence. $\overline{\alpha}_n/\overline{\lambda}_n$ is the contrast limit of fluorescence spin read out.

3. MLE and pMLE method

Before proposing a new solution, we can use the established model of the relationship between μ_n and P to analyze PS method from the perspective of mathematical statistics. It is assumed that each data point μ_n satisfies an independent Poisson distribution [3]. Then the PS method estimates P with the following formula:

$$\hat{P}_{PS} = \frac{\sum_{n=1}^{n=N}(\mu_n - \beta\Delta t\lambda_n)}{\beta\Delta t\sum_{n=1}^{n=N}\alpha_n}. \tag{14}$$

For the evaluation of the quality of the estimate, there are two indicators, unbiasedness and variance. For the PS method, it satisfies the unbiasedness, and its variance is:

$$\sigma_{PS}^2 = \frac{\sum_{n=1}^{n=N}F_n}{\beta\left(\Delta t\sum_{n=1}^{n=N}\bar{\alpha}_n\right)^2}. \tag{15}$$

Based on mathematical statistics theory, there is a lower bound of variance for all estimation methods of spin projection P [32]. This lower bound is called Cramér–Rao bound, which is the inverse of the Fisher information. The method saturating the Cramér–Rao bound is called the effective estimation, which is the optimal estimation. The Cramér–Rao bound is:

$$\sigma_{bound}^2 \approx \frac{1}{\beta\Delta t^2\sum_{n=1}^{n=N}\bar{\alpha}_n^2/F_n}. \tag{16}$$

According to (15) and (16), $\sigma_{PS}^2 \neq \sigma_{bound}^2$. Thus, the PS method is not the optimal estimation. By applying an understanding of fluorescence dynamics, an estimation method based on MLE for P is proposed. The proposed method entails the selection of P that maximizes the likelihood function. The formula for this process is,

$$\hat{P}_{MLE} = \arg\max L(P|\mu_1, \mu_2, \cdots, \mu_N). \tag{17}$$

Since μ_n satisfies the Poisson distribution, the probability density function and likelihood function of each measurement point is given by,

$$L(P|\mu_n) = P(\mu_n|P) = \frac{\left(\beta\Delta t\left(\bar{\alpha}_n P + \bar{\lambda}_n\right)\right)^{\mu_n}}{\mu_n!}e^{-\beta\Delta t\left(\bar{\alpha}_n P + \bar{\lambda}_n\right)}. \tag{18}$$

The total log-likelihood function is,

$$L = -\sum_{n=1}^{N}\beta\Delta t\left(\bar{\alpha}_n P + \bar{\lambda}_n\right) + \sum_{n=1}^{N}\mu_n\ln\left(\beta\Delta t\left(\bar{\alpha}_n P + \bar{\lambda}_n\right)\right) - \text{const}. \tag{19}$$

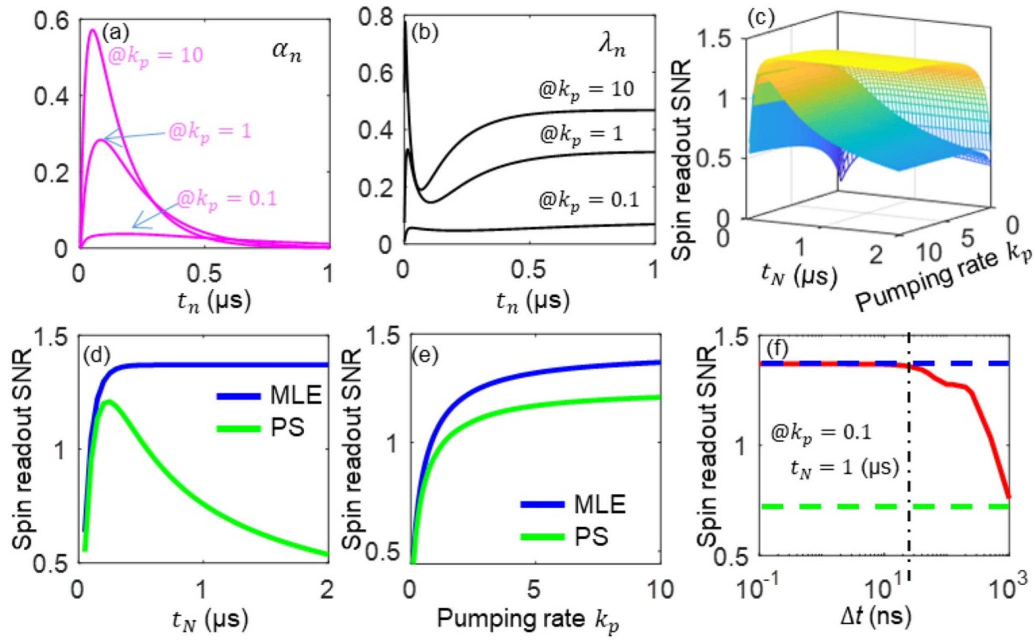

Figure 2. (a) Change of α_n with the time t_n under different pumping rate k_p. (b) Change of λ_n with the time t_n under different pumping rate k_p. (c) Two-dimensional plot of SNR as function of t_N and k_p. The SNR of the PS method (below) based on equation (23) and the MLE method (upon) based on equation (24), in which $\beta = 1$. The time interval Δt here is set to 0.1 ns. In order to clearly reveal the relationship between the SNR and (t_N, k_p) of the two methods, the two-dimensional plot is projected on t_N to obtain (d) the optimal SNR under different t_N and on k_p to obtain (e) the optimal SNR under different k_p. (f) The SNR of the MLE method changes with the interval time. The blue dotted line and the green dotted line represent the SNR of the MLE method with $\Delta t = 0.1$ ns and the PS method under the conditions of $k_p = 0.1$ and measurement time $t_N = 1$ μs in (c). The red solid line represents the change of the SNR of the MLE method with the interval time Δt under same condition.

The necessary condition to maximize L is,

$$\frac{\partial L}{\partial P} = 0. \tag{20}$$

It can be shown that the solution of equation (20) is also the solution of the following formula,

$$-\beta\Delta t\sum_{n=1}^{N}\bar{\alpha}_n + \sum_{n=1}^{N}\frac{\bar{\alpha}_n\mu_n}{\bar{\alpha}_n P + \bar{\lambda}_n} = 0. \tag{21}$$

Equation (21) is an Nth degree equation and is mathematically prohibitive, so is the standard deviation formula of the MLE method. However, the variance of the Gaussian distribution can be used to approximate the standard deviation of $\hat{P}_{MLE}$, (see appendix A for the solution process)

$$\sigma^2_{MLE} = \frac{1}{\Delta t^2\beta\sum_{n=1}^{n=N}\bar{\alpha}_n^2/F_n}. \tag{22}$$

The variance of the MLE scheme is equal to the lower bound, so it is the optimal estimation. The reason why the MLE method has a smaller variance than the PS method is explained as follows: as can be seen from equations (18)–(22), the difference between the MLE method and the conventional PS method is that MLE distinguishes the importance of data at different positions by the coefficient $\bar{\alpha}_n^2$ and F_n. A commonly used index in any metrology is the signal-to-noise ratio (SNR). Therefore, SNR is examined. SNR is defined as $SNR = \frac{|S_{P=1}-S_{P=0}|}{\sigma}$ which is the ratio of the range of spin readout signal to the standard deviation of the signal. The SNR of PS method is

$$SNR_{PS} = \Delta t\sqrt{\beta\frac{\left(\sum_{n=1}^{n=N}\bar{\alpha}_n\right)^2}{\sum_{n=1}^{n=N}F_n}}. \tag{23}$$

The SNR of MLE method is,

$$SNR_{MLE} = \Delta t\sqrt{\beta\sum_{n=1}^{n=N}\frac{\bar{\alpha}_n^2}{F_n}}. \tag{24}$$

According to equations (23) and (24), we can conduct a comparative analysis of MLE and PS schemes. For the parameters required by MLE, α_n and λ_n, as shown in figures 2(a) and (b), we observe the changes of α_n and λ_n with time under the conditions of three different optical pumping rates $k_p = 10$, 1, 0.1. It can be seen that α_n has a peak at about 100 ns and gradually tends to 0 as time increases, and λ_n tends to stabilize with time.

Different values of k_p and t_N are chosen to determine the optimal spin-readout SNR for both methods, and the results are shown in figures 2(c)–(e). For N, the SNR of the PS method has a peak at approximately 200 ns and then drops rapidly. This is due to the fact that μ_n later in time only contains noise inside of the spin information. For the MLE method, the μ_n later in time, through regulation of the small value of α_n, has little contribution to the estimation result. Therefore, long-term integration does not reduce the SNR. For the optical pumping rate, increasing the value of k_p is beneficial to improve the SNR for both methods. k_p is limited to a maximum value of 10 due to the limited laser power density in practical situation. As shown in figure 2(d), the SNR of the MLE method is increased by approximate 20% compared to the PS method. We also studied the effect of time interval on the SNR, as shown in figure 2(f). It can be seen that the time interval Δt of less than 10 ns will not substantially reduce SNR of the MLE method, but a time interval of more than 10 ns will obviously reduce the SNR. This could be explained as follows: the essence of the advantages of the MLE method over the PS method is the more efficient usage of information in μ_n. According to equation (19), for the MLE method, μ_n with a large $\bar{\alpha}_n/\bar{\lambda}_n$ ratio contributes more to the estimation result. For the PS method, all data contributes the same to the result. Therefore, the MLE method is better than the PS method. Increasing the time interval will lead to a decrease in the effective information. When the time interval Δt is as long as the total measurement time t_N, the MLE method degenerates into the PS method.

Since equation (21) is not easy to solve, a numerical solution algorithm for the solution of P is proposed, and the details are shown in appendix B. The algorithm solves $f(P,t)$ and calculates the corresponding likelihood function, and then searches $\hat{P}_{MLE}$ by a combination of rough global violent search and local dynamic programming search to achieve a faster search for the solution of $\hat{P}_{MLE}$ and eliminate the quantization noise caused by the discretization. Since k_p determines the values of α_n and λ_n, the estimation method requires the value of k_p in advance. To accomplish this, a fitting method for calculating k_p is proposed in appendix C.

Apart from photon shot noise, there are many sources of noise in the actual experimental process. These other sources of noise can cause the actual system to be unable to reach the photon shot noise sensitivity limit. For practical experimental systems, noise mainly include laser noise, detection noise, and noise in the light path. In this work, they are all considered as classic noise. The noise suppression method of PS mainly suppresses the common-mode noise of the system by using a differential method [33], which cannot completely suppress laser noise [34]. Moreover, in the summation method, β defaults to a fixed value, which means the detection noise cannot be effectively suppressed. To address this problem, a pMLE method is proposed here to improve the robustness of the estimation subject to classical sources of noise. The idea of pMLE is to estimate k_p, P, and β simultaneously. By using this approach, the system noise related term k_p and β can be separated from the spin-estimated signal. In order to achieve a simultaneous estimation of k_p, P, and β, a two-step estimation approach is proposed. In the first step, all possible (P, k_p) pairs are obtained. Next, the optimal β for each (P, k_p) pair is estimated as follows,

$$\hat{\beta}_{(P,k_p)} = \arg\max L(\beta\,|P,k_p,\mu_n) = \frac{F_n}{\bar{\mu}_n}. \tag{25}$$

In the second step, the likelihood function of each (P, k_p) pair is obtained by using the previously determined $\hat{\beta}_{(P,k_p)}$. The corresponding optimal (P, k_p) pair is then obtained using a second MLE. The estimated formula is as follows:

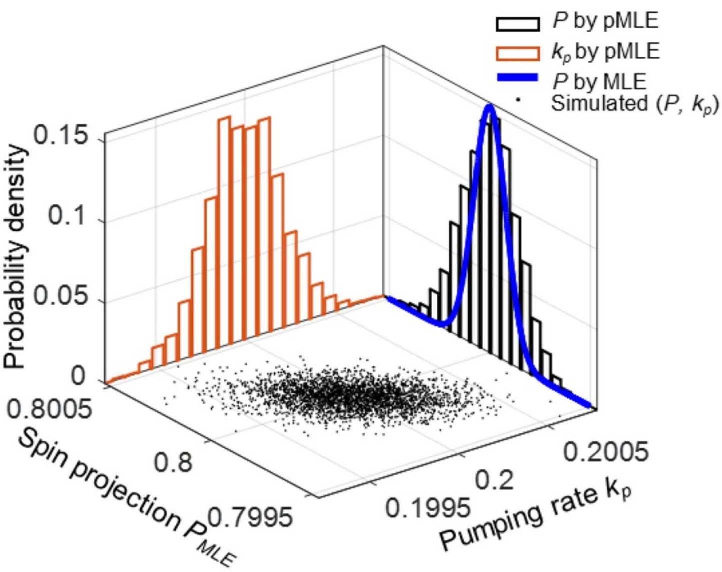

Figure 3. Results of the probability density function of the pMLE method obtained by Monte Carlo simulation with 3000 sample times. The blue curve represents MLE with k_p known in advance. The histogram represents the pMLE's probability density.

$$\left(\hat{P},\hat{k}_p\right)_{MLE} = \arg\max L\left(P,k_p\left|\hat{\beta}_{(P,k_p)},\mu_n\right.\right). \tag{26}$$

The equation is solved using the numerical solution algorithm shown in appendix B. From equations (25) and (26), it can be seen that the pMLE method, with the exception of the dynamic model of the NV center, does not depend on any prior information and only μ_n is necessary. However, since a set of data estimates the three parameters simultaneously, the accuracy of the P estimation is reduced, which is shown in figure 3. The estimation was performed using a fluorescence waveform corresponding to $(P = 0.8, k_p = 0.2)$. The results in figure 3 show that the accuracy degradation of the pMLE is 30.5% compared with the MLE method for P estimation. This shows that the SNR of pMLE is very close to the conventional PS shot noise limit. In order to further suppress the noise, a differential pMLE is proposed here by combining the differential PS method and pMLE method, in which P of the reference pulse is estimated simultaneously with P of the signal pulse, and then the difference is calculated.

4. Evaluation of MLE and pMLE

4.1. Simulation

Simulation is performed to analyze the pMLE method's classical noise suppression capability. The method of the simulation is to add noise of a specific frequency ω, and a specific root mean square (RMS) $\Delta/\sqrt{2}$ to the detection noise related factor, $\beta(t) = \beta(1+\Delta\sin(\omega t))$, or the laser power noise

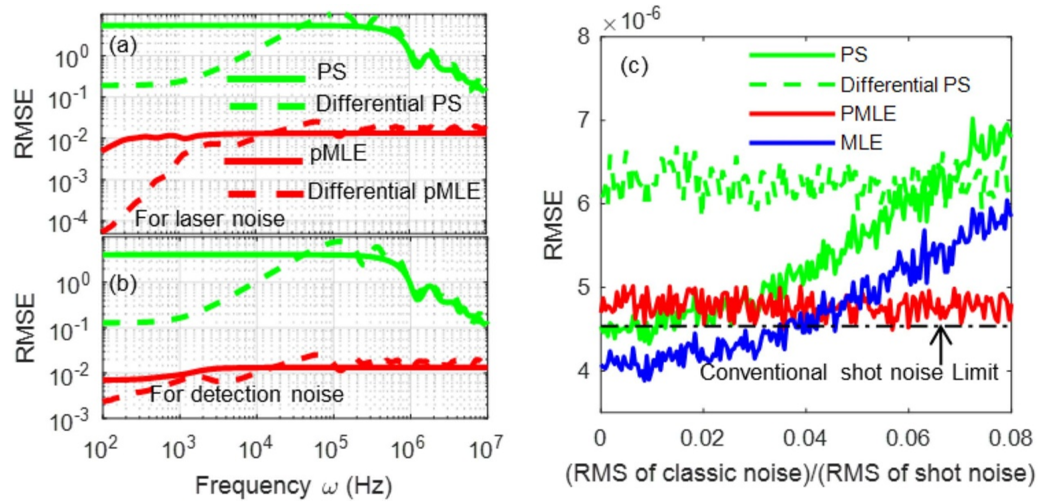

Figure 4. The suppression of different frequency noise using different spin readout schemes at $k_p = 0.2$. The vertical axis is the RMSE of the spin readout signal. The total sequence duration is 10 μs, corresponding to the sequence frequency $\omega_p = 10^5$ Hz. (a) The added classical noise is the detection noise. (b) The added classic noise is the laser noise. (c) The RMSE of the pMLE and MLE methods for different classical noise amplitudes is shown. Noise is generated by a white noise passing through a RC low-pass filter with a cutoff frequency of 10 kHz.

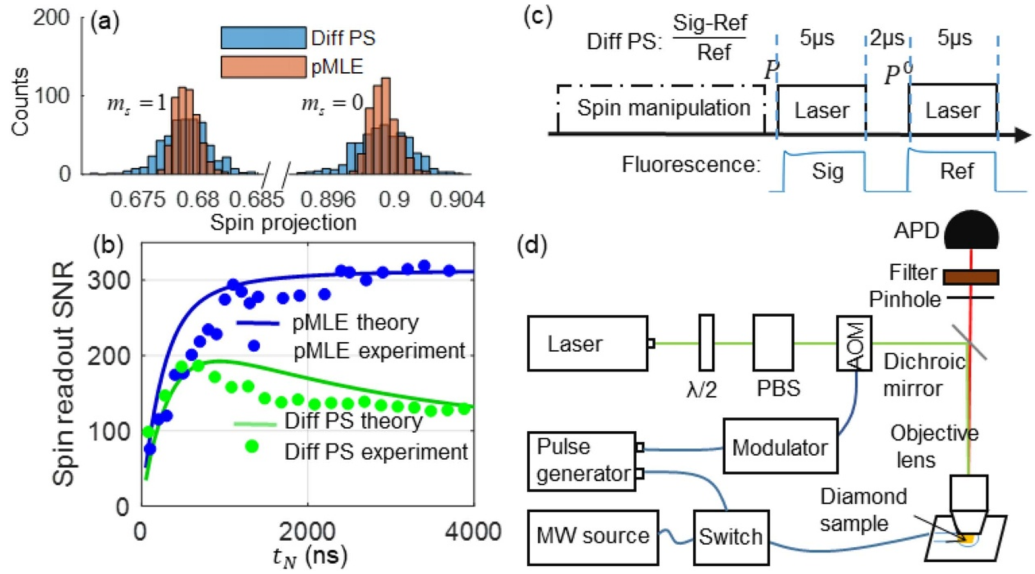

Figure 5. (a) Histogram of experimental spin readout results for differential PS method and pMLE method and $t_N = 2$ μs f or both methods. (b) SNR results of experiment verification. Both pulse lengths are 5 μs and the interval between the two pulses is also 2 μs. (c) The spin detection sequence, the first pulse is the signal pulse, and the second pulse is the reference pulse for differential detection. This ensures that the singlet completely relaxes to the ground state. In order to simulate the actual application scenario, the spin control section is added, and the total sequence pulse time is 14 μs. (d) Experiment setup schematic diagram.

related factor, $k_p(t) = k_p(1 + \Delta \sin(\omega t))$. Subsequently, the root mean square error (RMSE) of the output result is found. Namely, the noise suppression capability is observed at different frequencies. The results are shown in figures 4(a) and (b). The pMLE method has a similar ability for reducing the laser noise and detection noise. The results show that the PS method mainly suppresses the noise with a frequency higher than sequence frequency ω_p. ω_p is the reciprocal of the total time of one measurement pulse. Noise with a frequency much lower than ω_p can be suppressed by the differential PS method. However, noise with a frequency close to ω_p cannot be effectively suppressed. The present results show that the pMLE method can achieve effective noise suppression throughout the full frequency band. Compared with the PS method, the pMLE method improves the noise suppression near ω_p by nearly 300 times. For low-frequency noise, the pMLE method improves noise suppression by approximately 19 times compared with differential PS method at 100 Hz. Additionally, at this frequency, the differential pMLE can further improve the noise suppression by 55 times compared to that of the differential PS method.

From the above analysis, it can be found that the pMLE method is suitable for usage under classical noise conditions. As well, the MLE method is suitable for conditions where the photon shot noise is dominant. Thus, the conditions of usage for the various methods are analyzed. The results are shown in figure 4(c). When the amplitude of the classical noise's RMS is 4.5% of the photon shot noise or less, the MLE estimation accuracy is higher. Conversely, if the system noise is larger than 0.45% of the photon shot noise, the pMLE estimation accuracy is improved.

4.2. Experiment

In order to verify the present theory, an experimental verification was conducted. The experimental setup is shown in figure 5(d). The diamond sample used in this work was a high-pressure high-temperature type-Ib diamond (Element Six) under 5×10^{17} ea cm^{-2} with 10 MeV electron irradiation and 2 h annealing at 800 °C. The initial substitutional nitrogen concentration in the diamond was less than 200 ppm [35]. A homemade confocal experimental system was used for NV spin readout. The laser model was an Oxxius lcx-532 l-500, which has a maximum power of 500 mW and RMSE of approximately 0.2%. The objective lens is $60 \times$ /0.8NA and 0.17 mm working distance. An avalanche photodiode (Thorlabs APD120A2/M), which RMSE is less than 0.015%, was used for fluorescence detection. Under the experimental conditions, the steady-state voltage of the APD output was about 0.5 V, and the parameter $\beta \approx 500$ was calculated. The relative RMS of the photon shot noise was about 1%. The ratio of the classical noise to the quantum noise is larger than the criterion discussed in figure 4(c). Therefore, the pMLE method is used instead of the MLE method for the spin readout. For an actual NV ensemble system, considering the existence of NV^0, we add a fluorescence term proportional to k_p in the MLE solution algorithm to eliminate the effect of the spin estimation of NV^0 fluorescence. For the charge states transition dynamics between NV^0 and NV^-, we assume that the microwave manipulation duration on the order of microseconds is much shorter than the transition dynamics which is on the order of milliseconds [36, 37]. Therefore, in the spin readout process, the charge states dynamics is in equilibrium and the model does not need to add additional dynamic analysis of charge states dynamics. For comparison, a spin readout experiment was also performed using the differential PS method whose scheme is shown in figure 5(c). The experiment results are shown in figures 5(a) and (b) under the condition of $k_p = 0.195$. It can be seen from the experimental results that SNR of the PS method are consistent with the theoretical SNR. The theoretical SNR in figure 5(b) is lower than that in figures 2(c) and (d). This is because we have considered the laser gradient during the actual experiment. The gradient of the light spot excitation results in different pumping rates for the NV centers at different locations, which thereby reduces the accuracy of the estimation. See appendix D for the specific process of correcting the effect of laser spot gradient on SNR.

5. Conclusion

In summary, by solving the rate equation model, a method of spin readout based on the MLE of the fluorescence waveform was proposed. Compared with the PS method, the MLE method has a theoretical SNR limit that is 20% higher than the PS method. To account for the classical noise existing in practical applications such as quantum sensing, a pMLE method was proposed in order to separate optical noise and detection noise from the spin signal. Through simulation tests, this method was shown to increase the classical noise suppression capability by up to 300 times compared to the differential PS method. Using the pMLE method, the accuracy of the final estimation is close to the photon shot noise limit in the presence of ambient noise. The effectiveness of this method was verified experimentally. The present work shows that this method can improve spin detection accuracy and can be applied to pulse-based NV center sensing applications to achieve better sensitivity. In addition to improving the performance of the pulsed NV center spin readout, it is meaningful for improving the performance of general sense of pulsed spin readout.

Acknowledgments

This work was supported by the National Key R&D Program of China (2016YFB0501600); the Projects of National Natural Science Foundation of China under Grant Nos. 61773046 and 61721091; the Projects of Beijing Academy of Quantum Information Sciences under Grant No. Y18G33; Project funded by China Postdoctoral Science Foundation 2019M662121 and the Advanced Innovation Center of Big Data Precision Medicine of Beihang University.

Appendix A. Solution process of the MLE method

The Poisson distribution can be approximated by a Gaussian distribution when the number of photons is large [38]. Therefore, the standard deviation of the Poisson distribution can be approximated from the standard deviation of the Gaussian distribution, The maximum likelihood estimation result of the Gaussian distribution is solved as follows: First, the likelihood function of each data point is,

$$\begin{aligned} L(P|\mu_n)_{gauss} &= P(\mu_n|P)_{gauss} \\ &= \exp\left(-\frac{1}{2\sigma_n^2}\left(\beta\Delta t\left(\bar{\alpha}_n P + \bar{\lambda}_n\right) - \mu_n\right)^2\right). \end{aligned} \tag{A1}$$

Thus, the sum of the log-likelihood functions of all points is,

$$L_{gauss} = -\sum_{n=1}^{n=N} \frac{1}{2\sigma_n^2}\left(\beta\Delta t\left(\bar{\alpha}_n P + \bar{\lambda}_n\right) - \mu_n\right)^2. \tag{A2}$$

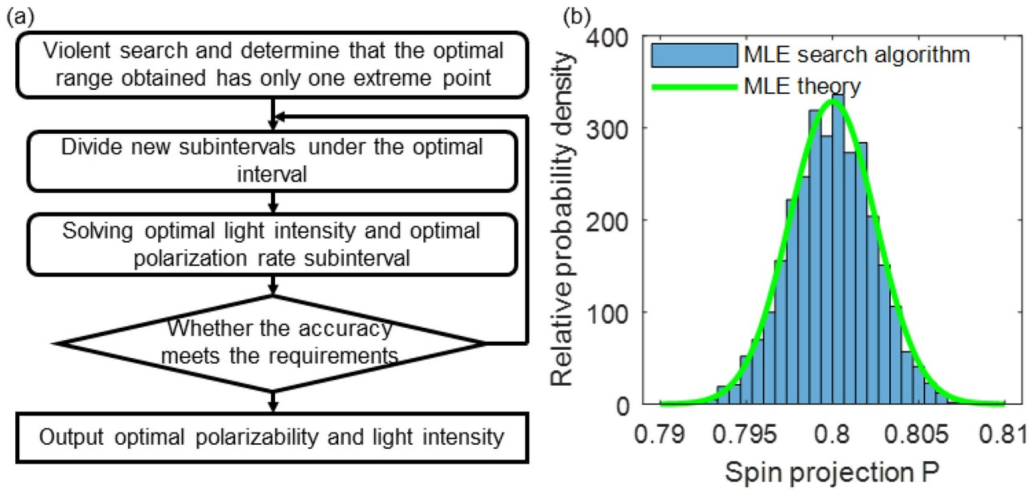

Figure A1. (a) MLE and pMLE solution algorithm flow chart. (b) The confidence interval of the method obtained by Monte Carlo simulation with 3000 sample times. The simulation conditions are pumping rates $k_p = 0.2$ and $\beta = 10^4$. The green line is the theoretical spin projection probability density distribution of MLE (a). The standard deviations are 0.0025. The histogram is the probability density distribution of the simulation of MLE method. The standard deviations are 0.0025.

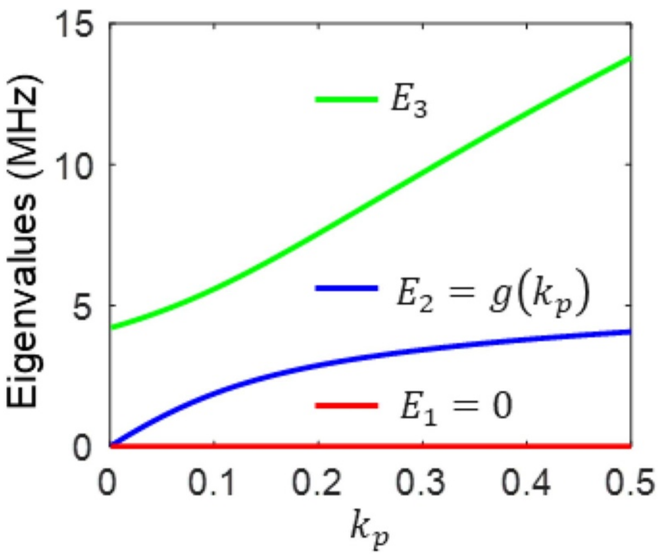

Figure A2. Relationship between k_p and eigenvalues.

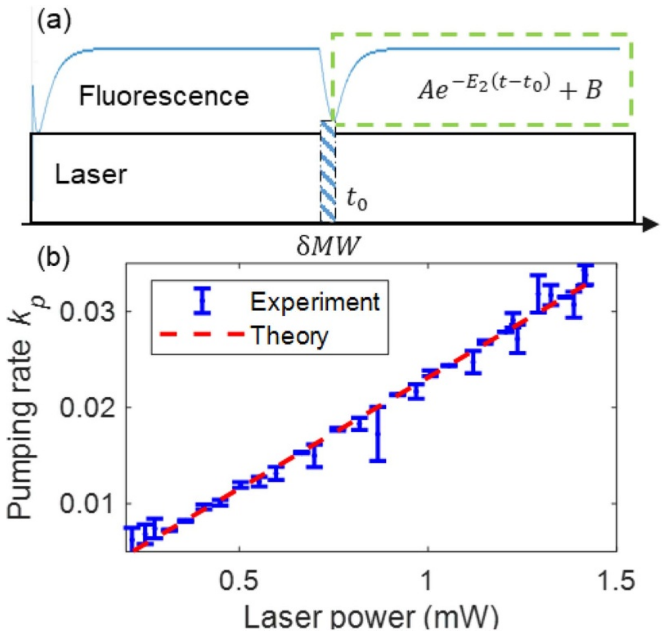

Figure A3. (a) Measurement sequence diagram. The lower half is the sequence, and the upper half is the simulated fluorescence response. (b) Experimental results.

From the principle of maximum likelihood, the spin projection value is given by the value corresponding to the maximum likelihood function,

$$\left(\hat{P}\right)_{gauss} = \arg\max L(P|\mu_n)_{gauss}. \tag{A3}$$

In order to find the maximum, a derivative of 0 is selected as equation (A2). The above formula is equivalent to,

$$\sum_{n=1}^{n=N} \frac{\overline{\alpha}_n}{\sigma_n^2}\left(\beta\Delta t\left(\overline{\alpha}_n P + \overline{\lambda}_n\right) - \mu_n\right) = 0. \tag{A4}$$

Subsequently, the solution of the maximum likelihood obtained by equation (A3) is given by,

$$\left(\hat{P}\right)_{gauss} = \frac{\sum_{n=1}^{n=N} \mu_n\overline{\alpha}_n/\sigma_n^2 - \beta\Delta t\sum_{n=1}^{n=N}\overline{\lambda}_n\bar{\alpha}_n/\sigma_n^2}{\beta\Delta t\sum_{n=1}^{n=N}\overline{\alpha}_n{}^2/\sigma_n^2}. \tag{A5}$$

The standard deviation of each measurement is:

$$\sigma_n^2 = \langle\mu_n\rangle = F_n\beta. \tag{A6}$$

The standard deviation of the Gaussion distribution is obtained as follows,

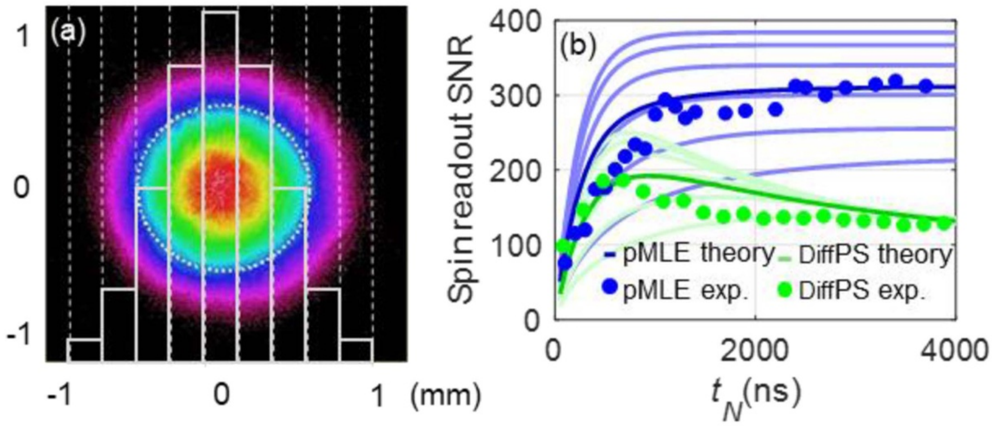

Figure A4. (a) Picture of laser spot distribution before the objective lens, which is obtained by a CCD camera. Because the experiment is a confocal scheme, the distribution of the spot before the objective lens is the same as that in diamond. In addition, the volume excited by the laser is mainly concentrated in a very thin layer, so only the lateral distribution needs to be considered. The laser spot follows a Gaussian distribution. Since the light spot is circularly symmetric, it is divided into 6 parts from the center to the periphery according to the laser power, as shown in the histogram. (b) Six SNR curves (PS method) of light green and six SNR curves (MLE method) of light blue correspond to six k_p values in figure A4(a). Dark blue curve and dark green curve represent modified SNR results of MLE and PS method, respectively.

$$\sigma_{MLE} = \frac{1}{\sqrt{\beta \Delta t^2 \sum_{n=1}^{n=N} \bar{\alpha}_n^2 / F_n}} \tag{A7}$$

Appendix B. Fast estimation result search algorithm

For the estimation of the spin projection and the optical pumping rate, the estimation range of the spin projection P is 0–1, and the estimated range of the optical pumping rate k_p is 0–1. Assuming that the estimated resolution is 10^{-8}, the number of calculations required for a full brute force search is about 10^{16}. This large number of calculations is far beyond the computing power of a personal computer. Therefore, a dynamic planning method is adopted in order to reduce the overall number of calculations as shown in figure A1(a). First, a global brute force search algorithm with an accuracy of 1/100 is used to determine the initial optimal range. Second, based on this range, the confidence interval is divided into three segments, and the optimal interval is solved. The process is then cycled, and the initial interval of each cycle is set as the optimal interval obtained from the last time step until the estimated resolution requirement is reached. Using this approach, a resolution of 10^{-8} is only required to be cycled 13 times. In this case, the total number of calculations was 3.9×10^5 times, which can be solved by the personal computer less than one second. The reason for the division into three segments is because the number of segments that minimize the number of calculations can be obtained using the natural logarithm and yields a nearest integer of 3.

The above operation ensures that the quantization noise due to the infinitely small resolution is lower than the photon shot noise limit. Therefore, when estimating spin projection only, the standard deviation of the method is consistent with calculation using the theoretical formula. Monte Carlo simulation was used to verify the validity of the present numerical method. The results are shown in the figure A1(b). The experimental results demonstrate that the present numerical approach can effectively achieve the same standard deviation as the theoretical approach.

Appendix C. Optical pumping rate fitting

Although the spin projection is to be estimated, the optical pumping rate k_p is also an important parameter for the analysis presented in this work. The algorithm of the analysis method in the present work is to find the optimal solution using a global violent search and local dynamic programming search algorithm. However, the time requirement of such an algorithm is high. The main reason for this is that the time required to perform a global search is high. Therefore, if the value of k_p can be confirmed in advance, the local greedy algorithm search can be performed directly and the complexity of the algorithm can be greatly reduced. Therefore, a method for measuring the optical pumping rate is proposed here.

The measurement idea is as follows. According to the analysis in Model, the optical pumping rate k_p and the relaxation rates k_{ij} jointly determine the eigenvalues of the characteristic matrix, A. Therefore, if the eigenvalues E_i can be found through experimental measurements, k_p can be found using the relationship between E_i and k_p. A measurement of only one of the five eigenvalues is necessary to fit for k_p. It can be calculated from A that E_1 is always 0 and that the value of E_3, E_4 and E_5 are much greater than k_pk, as shown in figure A2. The changes in

k_p have little or no effect on E_1, E_3, E_4 and E_5. Thus, the eigenvalue E_2 is the most suitable for this scheme as it is of a similar scale compared to the other eigenvalues. The relationship $g(k_p)$ between E_2 and k_p can be obtained by solving the eigenvalues of matrix A, but the solution is not suitable for fitting. We use a fourth-order polynomial fitting and k_p can be obtained from the following relation,

$$k_p = g^{-1}(E_2) = 0.003197E_2^4 - 0.01498E_2^3 + 0.03238E_2^2 + 0.02298E_2^1 + 0.003072. \tag{A8}$$

In order to experimentally measure the E_2 related exponential process, the sequence shown in figure A3(a) is used. First, a single laser pulse is inserted by a short microwave pulse, which is considered as an impulse. The laser before the microwave is long enough such that a steady-state is reached. At t_0, the microwave is applied while the laser is still activated. The microwave disrupts the steady-state of the ground state ρ_1 and ρ_2 but leaves the other three states steady. As a result, at t_0 after microwave pulse, the system reverts to an approximate steady-state polarization under the action of the laser, which is an E_2 related exponential process. The experimental results in figure A3(b) show a good linear relationship between the measured pumping rate and optical power, which is consistent with the theory.

Compared to the existing method for pumping rate measurement, which uses the saturation curve for analysis [39], the proposed method exhibits a higher accuracy at low pumping rates, which is a common operating condition of the laser.

Appendix D. Correction of laser spot gradient effect

In the theoretical derivation in MLE and pMLE method, k_p is considered to be a fixed value, which means that all NV centers are irradiated with laser light of the same intensity. In fact, due to the Gaussian distribution of laser light intensity, the participating NV centers cannot all be irradiated with laser light of the same intensity, that is, k_p is a distribution, not a constant value. As a result, the actual SNR is inconsistent with the theoretical SNR. To correct this deviation, we measured the spatial distribution of the laser spot as shown in figure A4(a). A simulation was performed on the distribution of k_p. In the simulation, we divided the light intensity into six values. As shown in the gray histogram shown in figure A4(a). The six light intensity values correspond to the SNR curves of light green (PS method) and light blue (MLE method) in figure A4(b), respectively. Summing the SNR corresponding to all k_p according to the weights gives a theoretical SNR that is in line with the actual situation, which is in good agreement with the actual situation, as shown by the dark green curve (PS method) and dark blue curve (MLE method) in figure A4(b).

ORCID iD

Jixing Zhang https://orcid.org/0000-0002-1983-5409

References

[1] Barry J F, Turner M J, Schloss J M, Glenn D R, Song Y, Lukin M D, Park H and Walsworth R L 2016 Optical magnetic detection of single-neuron action potentials using quantum defects in diamond *Proc. Natl Acad. Sci.* **113** 14133–8
[2] Wolf T, Neumann P, Nakamura K, Sumiya H, Ohshima T, Isoya J and Wrachtrup J 2015 Subpicotesla diamond magnetometry *Phys. Rev.* X **5** 41001
[3] Barry J F, Schloss J M, Bauch E, Turner M J, Hart C A, Pham L M and Walsworth R L 2020 Sensitivity optimization for nv-diamond magnetometry *Rev. Mod. Phys.* **92** 015004
[4] Fedotov I V, Blakley S, Serebryannikov E E, Safronov N A, Velichansky V L, Scully M O and Zheltikov A M 2014 Fiber-based thermometry using optically detected magnetic resonance *Appl. Phys. Lett.* **105** 261109
[5] Kucsko G, Maurer P C, Yao N Y, Kubo M, Noh H J, Lo P K, Park H and Lukin M D 2013 Nanometre-scale thermometry in a living cell *Nature* **500** 54–58
[6] Hall L T, Hill C D, Cole J H, Stadler B, Caruso F, Mulvaney P, Wrachtrup J and Hollenberg L C L 2010 Monitoring ion-channel function in real time through quantum decoherence *Proc. Natl Acad. Sci.* **107** 18777–82
[7] Schirhagl R, Chang K, Loretz M and Degen C L 2014 Nitrogen-vacancy centers in diamond: nanoscale sensors for physics and biology *Annu. Rev. Phys. Chem.* **65** 83–105
[8] Shao L, Zhang M, Markham M, Edmonds A M and Lončar M 2016 Diamond radio receiver: nitrogen-vacancy centers as fluorescent transducers of microwave signals *Phys. Rev. Appl.* **6** 064008
[9] Shao L, Liu R, Zhang M, Shneidman A V, Audier X, Markham M, Dhillon H, Twitchen D J, Xiao Y and Lončar M 2016 Wide-field optical microscopy of microwave fields using nitrogen-vacancy centers in diamonds *Adv. Opt. Mater.* **4** 1075–80
[10] Hopper A D, Shulevitz J H and Bassett C L 2018 Spin readout techniques of the nitrogen-vacancy center in diamond *Micromachines* **9** 437
[11] Xu L, Yuan H, Zhang N, Zhang J, Bian G, Fan P, Li M, Zhang C, Zhai Y and Fang J 2019 High-efficiency fluorescence collection for NV- center ensembles in diamond *Opt. Express* **27** 10787–97
[12] Momenzadeh S A, Stohr R J, De Oliveira F F, Brunner A, Denisenko A, Yang S, Reinhard F and Wrachtrup J 2015 Nanoengineered diamond waveguide as a robust bright platform for nanomagnetometry using shallow nitrogen vacancy centers *Nano Lett.* **15** 165–9
[13] Zhang C, Yuan H, Zhang N, Xu L X, Li B, Cheng G D, Wang Y, Gui Q and Fang J C 2017 Dependence of high density nitrogen-vacancy center ensemble coherence on electron irradiation doses and annealing time *J. Phys. D: Appl. Phys.* **50** 505104
[14] Herrmann J, Appleton M A, Sasaki K, Monnai Y, Teraji T, Itoh K M and Abe E 2016 Polarization-and frequency-tunable microwave circuit for selective excitation of nitrogen-vacancy spins in diamond *Appl. Phys. Lett.* **109** 183111
[15] Robledo L, Childress L, Bernien H, Hensen B, Alkemade P F and Hanson R 2011 High-fidelity projective read-out of a solid-state spin quantum register *Nature* **477** 574–8
[16] Gulka M *et al* 2017 Pulsed photoelectric coherent manipulation and detection of N−V center spins in diamond *Phys. Rev. Appl.* **7** 044032
[17] Dumeige Y *et al* 2013 Magnetometry with nitrogen-vacancy ensembles in diamond based on infrared absorption in a doubly resonant optical cavity *Phys. Rev.* B **87** 155202

[18] D'Anjou B and Coish W A 2014 Optimal post-processing for a generic single-shot qubit readout *Phys. Rev.* A **89** 012313
[19] Steiner M, Neumann P, Beck J, Jelezko F and Wrachtrup J 2010 Universal enhancement of the optical readout fidelity of single electron spins at nitrogen-vacancy centers in diamond *Phys. Rev.* B **81** 035205
[20] D'Anjou B, Kuret L, Childress L and Coish W A 2016 Maximal adaptive-decision speedups in quantum-state readout *Phys. Rev.* X **6** 011017
[21] Magesan E, Gambetta J M, Corcoles A D and Chow J M 2015 Machine learning for discriminating quantum measurement trajectories and improving readout *Phys. Rev. Lett.* **114** 200501
[22] Stürner F M *et al* 2019 Compact integrated magnetometer based on nitrogen-vacancy centres in diamond *Diam. Relat. Mater.* **93** 59–65
[23] Webb J L, Clement J D, Troise L, Ahmadi S, Johansen G J, Huck A and Andersen U L 2019 Nanotesla sensitivity magnetic field sensing using a compact diamond nitrogen-vacancy magnetometer *Appl. Phys. Lett.* **114** 231103
[24] El-Ella H A R, Ahmadi S, Wojciechowski A M, Huck A and Andersen U L 2017 Optimised frequency modulation for continuous-wave optical magnetic resonance sensing using nitrogen-vacancy ensembles *Opt. Express* **25** 14809–21
[25] Ma Z, Zhang S, Fu Y, Yuan H, Shi Y, Gao J, Qin L, Tang J, Liu J and Li Y 2018 Magnetometry for precision measurement using frequency-modulation microwave combined efficient photon-collection technique on an ensemble of nitrogen-vacancy centers in diamond *Opt. Express* **26** 382–90
[26] Liu Y *et al* 2020 Saturating the quantum Cramér-Rao bound and measuring the related quantum fisher information in a nitrogen-vacancy center in diamond in preparation (arXiv:2003.08373v1)
[27] Maze J R, Gali A, Togan E, Chu Y, Trifonov A, Kaxiras E and Lukin M D 2011 Properties of nitrogen-vacancy centers in diamond: the group theoretic approach *New J. Phys.* **13** 025025
[28] Doherty M W, Manson N B, Delaney P and Hollenberg L C L 2011 The negatively charged nitrogen-vacancy centre in diamond: the electronic solution *New J. Phys.* **13** 025019
[29] Goldman M L, Sipahigil A, Doherty M W, Yao N Y, Bennett S D, Markham M, Twitchen D J, Manson N B, Kubanek A and Lukin M D 2015 Phonon-induced population dynamics and intersystem crossing in nitrogen-vacancy centers *Phys. Rev. Lett.* **114** 145502
[30] Goldman M L, Doherty M W, Sipahigil A, Yao N Y, Bennett S D, Manson N B, Kubanek A and Lukin M D 2015 State-selective intersystem crossing in nitrogen-vacancy centers *Phys. Rev.* B **91** 165201
[31] Robledo L, Bernien H, Sar T V D and Hanson R 2011 Spin dynamics in the optical cycle of single nitrogen-vacancy centres in diamond *New J. Phys.* **13** 025013
[32] Jun S 2006 *Mathematical Statistics: Exercises and Solutions* (New York: Springer)
[33] Maze J R *et al* 2008 Nanoscale magnetic sensing with an individual electronic spin in diamond *Nature* **455** 644–7
[34] Zhang J, Yuan H, Zhang N, Xu L, Bian G, Fan P, Li M, Zhan Z and Yu K 2020 A modified spin pulsed readout method for NV center ensembles reducing optical noise *IEEE Trans. Instrum. Meas.* **69** 4370–8
[35] Zhang C, Yuan H, Zhang N, Xu L X, Li B, Cheng G D, Wang Y, Gui Q and Fang J C 2017 Dependence of high density nitrogen-vacancy center ensemble coherence on electron irradiation doses and annealing time *J. Phys. D: Appl. Phys.* **50** 505104
[36] Giri R, Gorrini F, Dorigoni C, Avalos C E, Cazzanelli M, Tambalo S and Bifone A 2018 Coupled charge and spin dynamics in high-density ensembles of nitrogen-vacancy centers in diamond *Phys. Rev.* B **98** 045401
[37] Giri R, Dorigoni C, Tambalo S, Gorrini F and Bifone A 2019 Selective measurement of charge dynamics in an ensemble of nitrogen-vacancy centers in nanodiamond and bulk diamond *Phys. Rev.* B **99** 155426
[38] Gupta A, Hacquebard L and Childress L 2016 Efficient signal processing for time-resolved fluorescence detection of nitrogen-vacancy spins in diamond *J. Opt. Soc. Am.* B **33** B28-B34
[39] Ahmadi S, El-Ella H A R, Hansen J O B, Huck A and Andersen U L 2017 Pump-enhanced continuous-wave magnetometry using nitrogen-vacancy ensembles *Phys. Rev. Appl.* **8** 034001